PAPER

Nitrogen-enriched porous carbon nanorods templated by cellulose nanocrystals as high performance supercapacitor electrodes†

Xinyun Wu,[a] Zengqian Shi,[a] Ricky Tjandra,[a] Aleisha Justine Cousins,[a] Serubbabel Sy,[a] Aiping Yu,*[a] Richard M. Berry[b] and Kam C. Tam*[a]

Cellulose nanocrystals (CNCs) for the very first time were converted into highly porous nitrogen (N)-doped carbon nanorods that display promising capacitive performance as electrode materials for supercapacitors. CNCs were used as both a carbon source and a template for the controlled-growth of the N precursor to form melamine-formaldehyde (MF) coated CNC nanorods (MFCNCs). The resulting hybrid material was further subjected to a one-step pyrolysis to yield N-doped carbon nanorods (N-MFCNCs) of high N doping content and favourable micro-, meso-, and macropores. An optimal capacitance of 328.5 F g^{-1} from the CV test at 0.01 V s^{-1} and 352 F g^{-1} from the CD test at 5 A g^{-1} was achieved for N-MFCNCs in sulfuric acidic electrolyte (1 M). The material also exhibits high cycling stability (less than 4.6% loss after 2000 cycles) at a high current density of 20 A g^{-1}. The versatility of the material was further demonstrated by high capacitive performance in neutral and alkaline electrolytes. Our work offers a promising alternative approach to fabricate high-performance nanostructured carbon from abundant biomass *via* facile and low-cost processing for energy storage applications.

1. Introduction

Supercapacitors (SCs) have received increasing attention because of the demand for future energy storage devices capable of delivering high power density with an extremely long cycle life. SCs are highly desirable for a wide range of applications including regenerative braking, hybrid electric vehicles, consumer electronics, uninterrupted power sources, and industrial power management.[1,2] Based on different charge storage mechanisms, there are two types of SCs: electrical double layer capacitors (EDLCs) and pseudocapacitors (PCs). For EDLCs, charge/discharge occurs at the electrode interface, while PCs store energy *via* reversible redox reactions on the surface of the active material. PCs typically offer higher energy density than EDLCs, however they suffer from poor cycling stability and retention capability which also resulted from the redox reactions. Therefore, EDLCs are still preferred industrially. The electrode material in today's commercial SCs mainly comprises active carbon due to its good electrochemical properties and relatively low cost.[3]

To enhance the energy density to the level of a secondary battery, there is significant effort and activity on increasing the surface area and porosity *via* advanced carbonaceous nanomaterials. Various carbon systems were proposed including activated carbon, carbide derived carbon, zeolite-templated carbon, carbon aerogel, onion-like carbon, carbon spheres, and carbon fibers are developed.[4–10] The well-controlled porous structure and high surface area achieved in the above systems have greatly enhanced the rate and capacitive performance of the carbon-based electrode material. However, achieving a high surface area and porosity often necessitate the use of complicated template synthesis and a tedious activation process. A further issue is that the conductivity decreases with increasing porosity.[11] Carbon nanotubes (CNTs) and graphene are two very attractive materials for high performance carbon-based SC electrode materials. Both have high electrical conductivity and exceptional theoretical surface area.[12–15] However, the production of good-quality CNTs and graphene is costly and achieving a high surface area is challenging due to aggregation and stacking. An alternative to enhancing the energy density of carbon-based materials is *via* heteroatom-doping with elements such as boron,[16–18] phosphorus,[19–21] sulphur,[22] and nitrogen (N)[23–29] into the carbon framework. A significantly higher specific capacitance (C_s) is achieved from enhanced electrochemical activity, such as higher conductivity and the PC effect. Improved wettability of porous carbons with electrolytes is also achieved *via* doping.[20,30–32]

[a]*Department of Chemical Engineering, Waterloo Institute for Nanotechnology, University of Waterloo, Waterloo, Ontario, N2L3G1, Canada. E-mail: aipingyu@uwaterloo.ca; mkctam@uwaterloo.ca*

[b]*CelluForce Inc., 625, Président-Kennedy Avenue, Montreal, Quebec, H3A 1K2, Canada*

Recently, nitrogen (N) doping has shown great promise, resulting in an enhanced capacitance while maintaining excellent cycling durability.[19,29,33–36] The superior doping effect of N is believed to be the attraction between five valence electrons and protons that enhances the charge density of the space-charge layer.[37] Two strategies are commonly used to introduce N into carbon matrices: post-treatment with bases, such as ammonium, amine, and urea; *in situ* doping with N-rich precursors. The first strategy normally results in surface doping with a relatively low N content[35,38–40] while the second typically results in a more efficient, higher and uniform N doping that also allows for the adjustment of the N content *via* controlling the pyrolysis conditions.[31,39–41] However, the second approach often involves the harsh etching of expensive templates such as mesoporous silica for the impregnation of N precursors after pyrolysis[41,42,44] or a time-consuming activation process, *via* direct carbonization of N-rich precursors, necessary for generating a good pore structure.[43,45] The production of carbonaceous electrode materials for SCs from biomass has attracted much interest[26,46–51] providing a sustainable and cost-effective starting material. However, to date, the carbon materials produced from biomass typically have a low surface area (<20 m² g⁻¹) and are non-porous in the absence of activation or templating.[52] Therefore, the task of developing carbon-based electrode materials with high surface area, porosity, and effective heteroatom doping using simple and cost effective methods still remains.

In this work, we report on the novel fabrication of N-enriched carbon nanorods (N-MFCNCs) with high surface area and porosity based on melamine formaldehyde coated cellulose nanocrystals (MFCNCs). CNCs extracted from wood fibers are typically 200 nm long and 2–5 nm in diameter, and they are good templates for the controlled-growth of MF on CNCs to yield core–shell-structured MFCNCs. The good water dispersibility of CNCs allows the individual coating of MF in aqueous solution. The production of hierarchically porous carbon nanorods and the required nitrogen doping were readily achieved through a one-step pyrolysis of MFCNCs without any activation process or the use of sacrificial templates. An optimal capacitance of 352 F g⁻¹ was obtained for the nitrogen-doped MFCNCs (N-MFCNCs) with robust cycling stability when 1 M sulfuric acid was used as the electrolyte. The superior supercapacitive behavior of N-MFCNCs was also demonstrated in neutral and alkaline electrolytes, indicating the versatility of N-MFCNCs as supercapacitor electrode materials. The enhancement in capacitance due to N doping becomes apparent when compared to the carbonized system based on pristine CNCs.[53] To the best of our knowledge, MF coated CNCs were synthesized for the first time and this is the first report of N-doped carbonized CNCs for supercapacitor application.

2. Experimental section

2.1 Materials

Cellulose nanocrystals (CNCs) were provided by FP Innovations and Celluforce Inc. All the chemicals used in this study were of analytical grade, purchased from Sigma-Aldrich, and used as received.

2.2 Synthesis of the melamine-formaldehyde (MF) precursor

In a typical synthesis, 2.2 g of melamine and 4.0 mL of formaldehyde (37% in water) were mixed in 10 mL deionized water in a 50 mL flask, followed by pH adjustment to be between 8 and 9 using NaOH solution. The temperature was increased to 80 °C under mechanical or magnetic stirring. The solution turns from cloudy to transparent within about 5 min. After 30 min, the precursor is ready for the next step.

2.3 Synthesis of melamine-formaldehyde cellulose nanocrystals (MFCNCs)

100 mL of 1% CNC suspension was mixed with the MF precursor from step 1, and the pH was adjusted to between 4 and 5 using HCl solution. The suspension was stirred for 2 h at 80 °C. During the process, the cross-linked melamine formaldehyde resin condenses on the CNC surface and forms a coating. The suspension was then allowed to cool to room temperature and purified by repeated filtration and washing with DI water. MF resin was synthesized under identical conditions in the absence of CNCs.

2.4 Carbonization of MFCNCs to N-MFCNCs

The nitrogen-doped carbonized MFCNCs (N-MFCNCs) were prepared by pyrolysis of freeze-dried MFCNCs in a quartz tube under a flow of argon at a desired temperature of between 800 and 1000 °C over 2 hours at 5 °C min⁻¹. N-MFCNCs carbonized at various temperatures are denoted as MFCNC800, MFCNC900, and MFCNC1000. After cooling to room temperature, N-MFCNCs were ground to fine powders.

2.5 Electrochemical characterization

Cyclic voltammetry (CV), charge and discharge (CD) measurements, and electrochemical impedance spectroscopy (EIS) were conducted using an electrochemical workstation (Zahner-Electrik, Germany) equipped with a three-electrode half-cell configuration with a platinum wire as the counter electrode. For tests in 2 M KCl, 6 M KOH, and 1 M H_2SO_4 electrolytes, Hg/HgCl, Hg/HgO, and Ag/AgCl were used as the reference electrodes, respectively. To fabricate the working electrode, the N-MFCNCs were dispersed and sonicated in a water/ethanol mixture (v/v = 50/50) to form an aqueous 2 mg ml⁻¹ ink. Then 10 μl of ink was pipetted twice onto the graphite carbon (GC) electrode (3 mm in diameter). The CV test was performed with scan rates between 1 and 400 mV s⁻¹. The capacitance obtained from the CV curve was calculated using the equation below:

$$C_s = \frac{\int i\,dV}{2 \times m \times \Delta V \times S} \qquad (1)$$

where C_s is the specific capacitance, $\int i\,dV$ is the integrated area of the CV curve, m is the mass of the active material, ΔV is the potential range, and S is the scan rate. The cycling stability was

This journal is © The Royal Society of Chemistry 2015

J. Mater. Chem. A, 2015, **3**, 23768–23777 | 23769

measured with the same experimental setup at a scan rate of 100 mV s^{-1}. Charge and discharge (CD) tests were performed by applying a constant current density between 5 and 20 A g^{-1}. The cell capacitance was determined from the CD curve using the equation given below:

$$C_s = I \Big/ \left(\frac{dV}{dt} \right) \qquad (2)$$

where $dV \, dt^{-1}$ was calculated from the first half slope of the CD discharge curve,[54] and I is the charge current density (A g^{-1}). The energy and power densities of MFCNC 900 were determined from the galvanostatic results based on eqn (3) and (4):

$$E = \frac{1}{2} \times C_s \times (\Delta V)^2 \qquad (3)$$

$$P_{av} = \frac{E}{\Delta t} \qquad (4)$$

where E is the energy density, ΔV is the potential range, P_{av} is the average power density, and Δt is the discharge time. Cycling stability was measured with the same testing setup at 20 A g^{-1}. Electrochemical Impedance Spectroscopy (EIS) was performed in the frequency range of 0.1 Hz to 200 kHz at an open circuit potential with an AC amplitude of 5 mV.

2.6 Physical and chemical characterization

The morphology of MFCNCs and N-MFCNCs was characterized using a Philips CM10 transmission electron microscope (TEM) and a JEM-2100 High resolution TEM. The CNC sample was stained with 2% (w/w) uranyl acetate negative stain for high resolution imaging. The surface charge of the MFCNCs and CNCs was measured using a Malvern Zetasizer Nano ZS (Worcestershire, UK) where the zeta potential of the particles was calculated from the electrophoretic mobility values using the Smoluchowski equation. The coating of MF on CNCs was further confirmed and characterized by FT-IR (PerkinElmer 1720 FT-IR spectrometer). For the FT-IR spectrum, freeze-dried samples were mixed with KBr and then compressed into pellets for measurements at a resolution of 4 cm^{-1}. The composition of the synthesized MFCNCs was estimated from thermal gravimetric analysis (TGA) by assuming that the thermal degradation process of MFCNCs is exactly the same as those of CNCs and MFCNCs. Samples of MFCNCs, CNCs and MF were placed in an inert ceramic crucible and heated from 25 to 800 °C at a heating rate of 10 °C min^{-1} with a flow of N_2 of 20 ml min^{-1}. X-ray diffraction (XRD) was performed with a Rigaku D/MAX-RB diffractometer using filtered Cu Kα radiation. The analysis of the surface area, pore diameter and volume was determined by N_2 adsorption analysis with an autosorb iQ-AG instrument (Quantachrome Co., USA) at 77 K using the multipoint BET (Brunauer–Emmett–Teller) model to eliminate any interference from weakly adsorbed species. Prior to measurements, the samples were degassed overnight at 150 °C under vacuum. Raman scattering spectra were recorded with a HORIBA Scientific LabRAM HR system (532.4 nm laser).

3. Results and discussion

The schematic of the preparation of N-MFCNCs is shown in Fig. 1. The MF precursor was mixed with CNCs to allow for the *in situ* polycondensation on the surface of CNCs. Then the core–shell structured MFCNCs were carbonized to N-MFCNCs at various temperatures. This synthesis is simple in terms of the procedure and apparatus, and it is highly efficient and industrially scalable.

To confirm the presence of MF in the MFCNC system, FTIR spectra were acquired and compared with those of MFCNCs and CNCs (Fig. 2(a)). Several peaks in the MFCNC spectrum are absent in the CNC spectrum. The new peaks are due to the 1,3,5-triazine ring (at 1556 and 812 cm^{-1}) and the methylene C–H bending vibration (at 1330 cm^{-1}) of melamine.[55] Further evidence was provided by zeta potential measurements, where pristine CNCs with a zeta-potential of -54 mV were dramatically increased to $+35 \text{ mV}$ for MFCNCs, suggesting the good coverage of MF on the surface of CNCs.

The MF content in the composite material was determined by thermogravimetric analysis (TGA), shown in Fig. 2(b). The thermodegradation curves showed that the residue at 600 °C was 14.6% for CNCs, 25.6% for MFCNCs, and 33.5% for pure MF resin. From this information, the MF resin content in MFCNCs was calculated to be 43.4% based on the following equations:

$$C_{CNC} + C_{MF} = 1 \qquad (5)$$

$$0.146 C_{CNC} + 0.4 C_{MF} = 0.256 \qquad (6)$$

where C_{CNC} is the content of CNCs in MFCNCs, and C_{MF} is the content of MF in MFCNCs.

The synthesized MFCNCs were directly imaged using TEM (Fig. 3(a)–(c)). CNCs without staining are very lightly colored in TEM images due to their low density. A more defined edge was shown in Fig. 3(b) for stained CNCs, and the typical diameter was observed to be around 6 nm. MFCNCs, however, appear much darker in color (Fig. 3(c)) with a noticeable increase in diameter to around 25 nm, indicating the successful coating by the MF resin. The hybrid material preserves the rod-shape of the CNCs with a smooth and thick MF surface. MFCNCs after synthesis remain well dispersed in solution and appear milky. TEM images of MFCNCs after carbonization at various temperatures are shown in Fig. 3(c)–(e). By increasing the temperature of pyrolysis from 800 to 900 °C, N-MFCNCs show a slight shrinkage in diameter while maintaining a well-defined shape. However, a further increase in the carbonization temperature to 1000 °C resulted in some structural breakdown which is shown in Fig. 3(f).

The degree of graphitization of all N-MFCNCs was investigated with an XRD (Fig 4(a)). The peaks at 2 theta = 18.5° and 40° are most relevant in assessing carbonization. These peaks showed that N-MFCNCs consisted of graphitized carbon after carbonization. In particular, increasing the temperature from 800 to 900 °C increased the peak intensity, suggesting a higher degree of graphitization at higher temperature. When the

23770 | *J. Mater. Chem. A*, 2015, **3**, 23768–23777

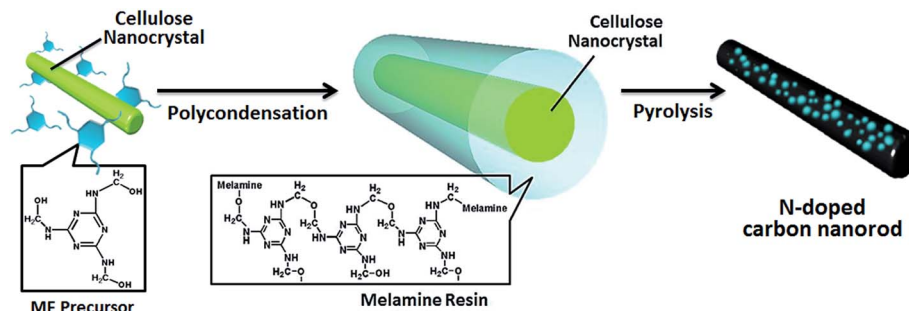This journal is © The Royal Society of Chemistry 2015

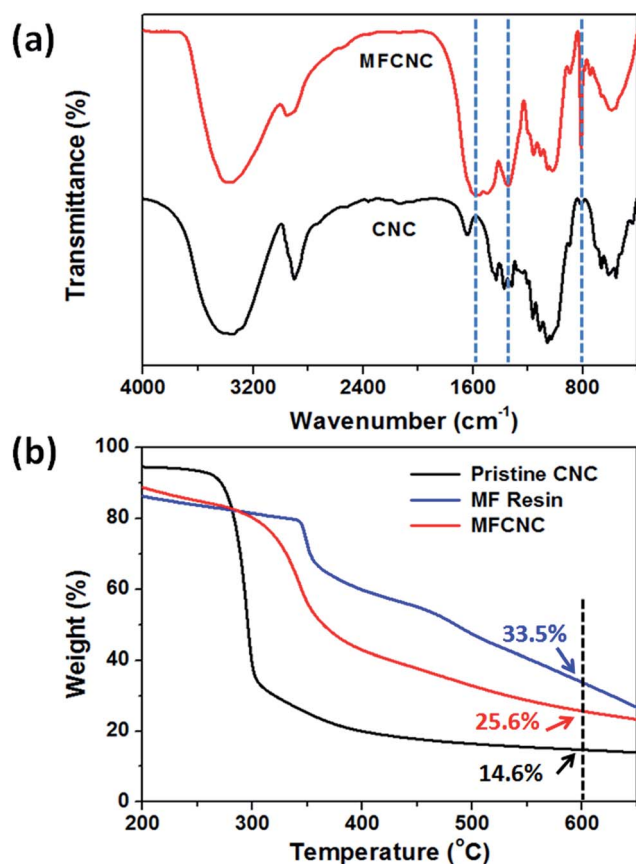Fig. 1   Schematic of the 2-step synthesis of nitrogen-doped carbon nanorods.

Fig. 2   (a) FTIR characterization of the freeze-dried MFCNCs and CNC powder, and (b) TGA measurement of MF resin, MFCNCs and CNCs under N_2.

the D peak relative to that of the G peak (I_D/I_G) is related to the amount of defects in the carbon materials.[56] By increasing the pyrolysis temperature from 800 to 900 °C, there was a decrease in I_D/I_G from 1.13 to 1.06 presumably due to both an increase in graphitization degree and a decrease in the nitrogen doping content.[57] A sharp increase to 1.14 in the ratio of the D to G bands was observed when the temperature was increased to 1000 °C, indicating a higher amount of disorder and defective sites introduced to the carbon structure. This is in good agreement with the TEM micrographs which revealed many structural defects in the samples carbonized at 1000 °C (Fig. 3(f)).

Since the carbonization temperature can significantly affect the physical and chemical properties of the carbon material, the composition, pore structure, and surface area were carefully investigated for N-MFCNC samples prepared at 800, 900 and 1000 °C respectively. The last 2 rows of Table 1 summarize the composition by elemental analysis of MFCNCs before and after pyrolysis showing the efficient nitrogen doping with melamine coated CNCs. The nitrogen doping depends on the pyrolysis temperature: 15.6% for MFCNC800, 8.45% for MFCNC900 and 4.28% for MFCNC1000. The reduced nitrogen content with increased temperature is in good agreement with previous studies and the phenomenon was proposed to be due to the evolution of nitrogenous volatile products such as HCN.[58–60] The texture of the material described by the pore size distribution (PSD), pore volume, and pore type is a critical for the super-capacitor performance and this is greatly affected by the carbonization temperature. To investigate the temperature effects on porosity, PSD curves and isotherms were developed and the results were plotted and summarized in Fig. 5 and Table 1.

The isotherms of all samples exhibited the representative type III behaviour defined by IUPAC with a H_3 type hysteresis loop. The sharp capillary condensation step at high relative pressures $P/P_0 > 0.90$ suggests the existence of large mesopores and macropores as indicated in the PSD graph. Moreover, MFCNC900 displayed a noticeable increased adsorption in the low pressure region suggesting the existence of micropores,[9,61] while in the case of MFCNC800 and MFCNC1000, almost no adsorption was observed. The observation is in agreement with the results summarized in Table 1, MFCNC900 possessed an optimal pore structure with the largest specific surface area of 564.2 m^2 g^{-1} that contributed to the improved capacitive

temperature reached 1000 °C, both peaks were significantly quenched due to the poorly organized carbon structure (also supported by TEM observation), which will also affect the electrochemical performance. Raman spectrometry is a sensitive technique to investigate the structural defects in carbon systems and was performed on all the N-MFCNC samples. Two peaks at 1350 and 1590 cm^{-1}, corresponding to the D and G bands of carbon materials, can be observed in the Raman spectra of all N-MFCNC samples (Fig. 4(b)). Since the D band changes with defects in the graphitic structures, the intensity of
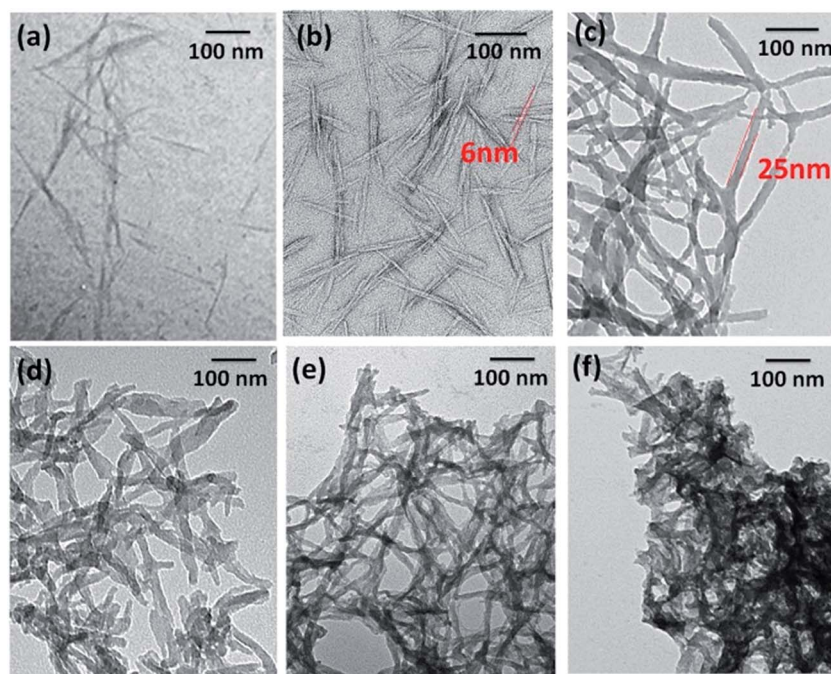
Fig. 3 (a) TEM image of pristine CNCs, (b) high resolution TEM image of pristine CNCs with uranyl acetate staining, and TEM images of (c) MFCNCs, (d) MFCNC800, (e) MFCNC900, and (f) MFCNC1000.
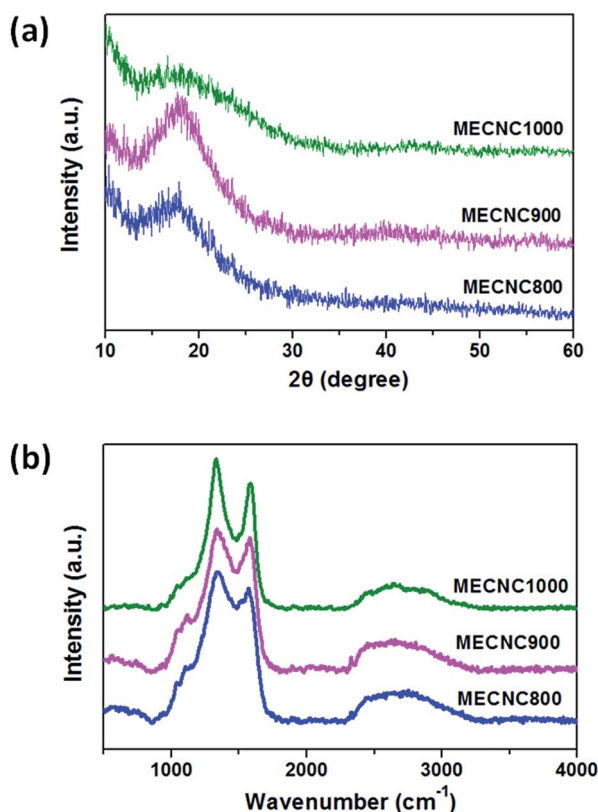

Fig. 4 (a) XRD and (b) RAMAN spectra characterization of N-MFCNCs prepared at various carbonization temperatures.

performance both EDLC and PC devices due to enhanced interactions with the electrolyte. Compared to MFCNC800, the increase in V_{total} is mainly attributed to the development of mesopores as indicated in the PSD graph where both micropores and mesopores are much better developed with intensified peaks at 1.5 nm, 2.5 nm and in the 4–5 nm region. Compared with MFCNCs without annealing, N-MFCNC samples carbonized at 800 and 900 °C showed an apparent increase in the surface area and a better developed pore structure. A sharp decrease in V_{total} and surface area was observed for MFCNC1000 which is mainly attributed to the destruction of the rod structure causing pore blockage (which is in agreement with the TEM observation). It is evident in the PSD curve that some isolated peaks from MFCNC800 and MFCNC900 merged into a much broader peak that decreased significantly in intensity. For example, the peaks at 2.5 nm and 4 nm for MFCNC900 became a broad weak peak at 3.3 nm. It has been demonstrated that a hierarchy of pores enhances the capacitance in several ways:[62,63] the macropores may serve as ion-buffering reservoirs, shortening the diffusion path to the interior pore surface; the mesopores may reduce the ion transport resistance and the micropores may enhance the EDLC capacitance. Therefore, MFCNC900 with an optimal hierarchical porous structure and a moderate N-doping content is expected to be the most favourable system for supercapacitor applications.
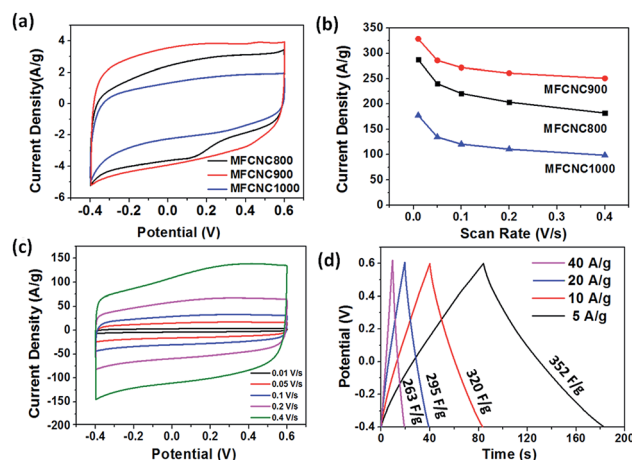
To confirm this, a series of electrochemical tests were conducted and the results are presented below. The electrochemical performances of the N-MFCNCs were investigated in a three electrode cell with a 1 M sulfuric acid aqueous electrolyte. The CV curve of N-MFCNC samples carbonized at various temperatures all demonstrated a quasi-rectangular shape which

23772 | *J. Mater. Chem. A*, 2015, **3**, 23768–23777

This journal is © The Royal Society of Chemistry 2015

Table 1 Summary of physicochemical characterization by BET and the composition of various N-MFCNCs by elemental analysis

	MFCNC	MFCNC 800	MFCNC 900	MFCNC 1000
BET surface area ($m^2\ g^{-1}$)	212.8	358.9	564.2	97.5
Total pore volume ($cm^3\ g^{-1}$)	0.07	0.50	2.03	0.40
Mean pore diameter (nm)	1.34	2.00	1.65	1.93
N content (%)	34.73	15.60	8.45	4.28
C content (%)	38.09	68.59	75.53	83.65
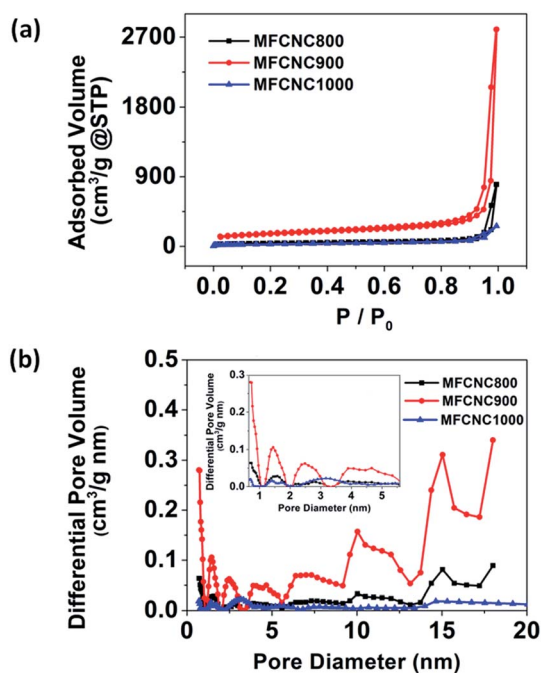
Fig. 5 (a) N_2 adsorption/desorption isotherms and (b) the corresponding PSDs of samples carbonized at different temperatures.

Fig. 6 (a) Cyclic voltammetry curves of MFCNC800, MFCNC900 and MFCNC1000 with the same scan rate of 0.01 V s^{-1}; (b) capacitance retention profiles with increasing scan rates for MFCNC800, MFCNC900 and MFCNC1000; (c) cyclic voltammetry curves of MFCNC900 at various scan rates; and (d) charge/discharge curves of MFCNC900 at various current densities.

suggests the combined effect of double-layer capacitor and pseudo-capacitive mechanisms in our system (Fig. 6(a)). The deformation of the CV curve at higher voltages is mainly due to the heteroatoms present in the carbon frame that cause a surface polarity phenomenon. MFCNC900 possesses the best C_s approaching 328.5 F g^{-1} at a 0.01 V s^{-1} sweep rate, followed by 287.3 F g^{-1} and 177.5 F g^{-1} for MFCNC800 and MFCNC1000, respectively. The prominent redox hump along the current–potential axis at 0.1–0.2 V for MFCNC 800 is due to the faradaic reaction from richer nitrogen functionalities. The presence of nitrogen in the carbon frame introduces basicity to the carbon framework that will further enhance the interaction with the acidic electrolyte. The overall good capacitive behavior of all N-MFCNCs is due to the combined contribution of double layer capacitance from high surface area and the pseudocapacitance from N functionality. N doping also increases conductivity and improves wettability that further enhance the supercapacitive performance.[16,64] It is worth noting that the capacitance of MFCNC900 surpasses the other two samples despite the lower N content of the MFCNC800, which shows the crucial role that the hierarchical porous structure plays in supercapacitor performance. Moreover, the relationship

between scan rate and capacitance (Fig. 6(b)) suggests good capacitance retention when the scan rate was increased from 0.01 V s^{-1} to 0.4 V s^{-1}, indicating efficient charge transfer kinetics. As shown in Fig. 6(c), the CV curve preserves its shape even at an increased scan rate up to 0.4 V s^{-1}. Further increasing the carbonization temperature from 900 to 1000 °C, however, results in a significant reduction in the capacitance due to the loss in N-doping, surface area, and pore structure. We further compared our results with various N-enriched carbon materials presented in recent years (summarized in Table 2)[36,58,65–68] on C_s and other major characteristics including electrolytes and the electrode material. Remarkably, our MFCNC 900 exhibits much a higher C_s value than those of reported systems. The overall excellent performance is attributed to the combined effect of a high nitrogen doping level (greatly improving the electronic properties and wettability of the material) as well as a well-developed porous structure and a high surface area (enhancing the accessibility of the electrolyte and facilitating the electron/ion transport).

To further investigate the supercapacitive behavior of MFCNC900, CD characterization within the same voltage window as CV tests was performed at 5 A g^{-1}, 10 A g^{-1}, and 20 A g^{-1} and the results are given in Fig. 6(d). The obtained profile is approximately linear with a slight curvature due to the faradaic reaction, implying that the material is behaving as a capacitor

This journal is © The Royal Society of Chemistry 2015

J. Mater. Chem. A, 2015, **3**, 23768–23777 | 23773

Table 2 Comparison of the C_s value of various N-doped carbon systems reported in recent years

Electrode Material	C_s (F g^{-1})	Electrolyte	Reference
Nitrogen-doped porous carbon nanofibers from bacterial cellulose	202	6 M KOH	65
Nitrogen-doped porous hollow carbon spheres	213	6 M KOH	66
Hierarchical nitrogen-doped carbon nanocages	313	6 M KOH	36
Hierarchical porous nitrogen-doped carbon nanosheets from silk	242	EMIMBF$_4$	67
N-doped multiwalled carbon nanotubes	167	1 M H$_2$SO$_4$	68
Melamine-based carbon	205	1 M H$_2$SO$_4$	58
This work	352	1 M H$_2$SO$_4$	

with high charge and discharge efficiencies. The capacitance was calculated to be 352 F g^{-1}, 320 F g^{-1}, 295 F g^{-1}, and 263 F g^{-1} at high charge/discharge rates of 5 A g^{-1}, 10 A g^{-1}, 20 A g^{-1}, and 40 A g^{-1}, respectively. In spite of the lower surface area compared with another reported carbonized CNC system using the more challenging silica template approach[53] (546 m^2 g^{-1} *versus* 400 m^2 g^{-1}), our N-MFCNCs still yield excellent C_s (352 F g^{-1} at 5 A g^{-1} *versus* 170 F g^{-1} at 0.23 A g^{-1}). This comparison further demonstrates the crucial role of introducing N-functionality in enhancing electrochemical properties. The specific energy density and power density were further calculated from the CD characterization. The excellent energy density approaches 48.8 W h kg^{-1} at a current density of 5 A g^{-1} and is maintained at a rather impressive value of 36.5 W h kg^{-1} at a current density of 40 A g^{-1}. The value is significantly higher than that of commercial carbon supercapacitors which is in the range of 4–5 kW h kg^{-1}.[69] Furthermore, the high power density of 39.85 kW kg^{-1} was achieved at a current density of 40 A g^{-1} which is almost twice the power target of the PNGV (Partnership for a New Generation of Vehicles) which is 15 kW kg^{-1}.[63]

Since cycling stability is a critical issue for most of the pseudocapacitive electrode materials due to material degradation from irreversible faradaic redox reactions, the stability test was conducted at a harsh charge–discharge rate of 20 A g^{-1} for 2000 cycles for MFCNC900. From the results shown in Fig. 7(a), the capacitance loss was only 4.6% even at such a high current density, indicating a durable structure and an efficient ion transfer mechanism for MFCNC900. EIS testing of all C-MFCNC samples was performed to elucidate the capacitive behavior and the results are shown in Fig. 7(b). A much steeper linear slope in the low frequency region was observed for MFCNC900 compared to the other two samples demonstrating an ideal capacitive behavior with the lowest ion diffusion resistance.[70] To support our observation, a detailed analysis for estimating the diffusion constant for the three samples was conducted. The Warburg plot showing the relationship between Z_{im} and $\omega^{-1/2}$ in the low-frequency region was obtained and is shown as the inset of Fig. 7(b). The slope of the fitted line corresponds to the Warburg factor (Ω cm^2 S$^{1/2}$) based on the relationship below:[71]

$$Z_{Re} \propto \sigma \omega^{1/2} \qquad (7)$$

where σ is the Warburg factor, and ω is the angular frequency. The fitting of the data shows that the magnitude of the slope follows the trend of MFCNC800 (115.18) > MFCNC1000 (77.76) >

MFCNC900 (19.85). The diffusion coefficient of ions D (cm^2 s^{-1}) in the electrolyte can be further estimated based on the equation below and it is inversely proportional to the Warburg factor:[71]

$$D = R^2 T^2 / 2A^2 n^4 F^4 C^2 \sigma^2 \qquad (8)$$

where R is the gas constant, T is the absolute temperature (298 K in our experiment), A is the surface area of the electrode (0.7065 $\times 10^{-6}$ m^2) based on a working electrode, 3 mm in diameter, n is the number of electrons per molecule during oxidization, F is the Faraday constant, and C is the concentration of ions in the electrolyte. From eqn (8), the diffusion coefficient D (cm^2 s^{-1}) can be resolved for the three samples and it follows the order of MFCNC800 (3.34 $\times$ 10^{-11}) < MFCNC1000 (7.34 $\times$ 10^{-11}) < MFCNC900 (1.13 $\times$ 10^{-9}). The results proved that the MFCNC900 has the most favourable diffusion rate (or lower
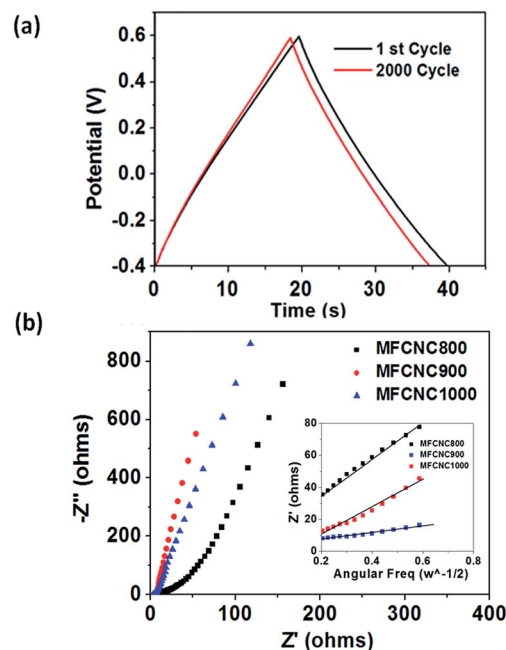

Fig. 7 (a) Stability test for MFCNC900 at 20 A g^{-1} charge/discharge rate for 2000 cycles, and (b) electrochemical impedance spectroscopy spectra of MFCNC800, MFCNC900 and MFCNC1000 under an AC voltage of 5 mV. The inset shows the relationship between Z_{im} and $\omega^{-1/2}$ in the low-frequency region.

diffusion resistance) primarily due to the most optimal porous structure.

To further explore the versatility of our N-MFCNCs, we performed series of electrochemical tests in two other common electrolytes – 2 M KCl and 6 M KOH. Excellent performance was also observed for MFCNC900 showing capacitances of 237.2 F g^{-1} and 289.5 F g^{-1} in neutral and alkaline electrolytes, respectively (a summary of capacitance performance in various electrolytes is shown in Table S1†).

The capacitance performance of N-MFCNC samples follows the same order in all three electrolytes: MFCNC900 > MFCNC800 > MFCNC1000. It was found that the CV curve of MFCNC900 in a neutral electrolyte displays the most rectangular shape (Fig. S1(a)†), suggesting that the contribution for capacitance in a neutral electrolyte is mainly from the EDLC mechanism. Therefore, the overall capacitive performance is lower in acidic and basic electrolytes due to the lack of pseudocapacitance. Further evidence is revealed in CV curves of various N-MFCNC (Fig. S1(c) and (d)†). No visible redox peaks were evident in any of the three N-MFCNC samples when tested in a neutral electrolyte, while the CV curves of both MFCNC800 and MFCNC900 in a basic electrolyte exhibited obvious peaks due to the faradaic contribution from the nitrogen functionalities. However, MFCNC900 in a neutral electrolyte demonstrates better cycling stability compared to that in acidic (4.6% loss) and alkaline electrolytes (4.3% loss); no capacitance loss over 2000 cycles was observed at the fast charge and discharge rate of 20 A g^{-1}. This trend in cycling stability is to be expected for N-MFCNCs in different types of electrolytes as it should follow the degree of faradaic reaction. The strong performance in the neutral electrolyte originates primarily from the electrostatic nature of the charge storage for double layer capacitors, while the basicity of MFCNCs resulting from nitrogen functionality enhances the pseudocapacitive performance *via* the faradaic reaction in an acidic solution.[72,73]

4. Conclusions

The synthesis of highly-porous N-enriched carbon nanorods was reported. Cellulose nanocrystals were used both as the carbon source and the template to facilitate the controlled growth of the nitrogen precursor into core–shell structured MFCNC nanorods. The abundant micro-, meso-, and macropores in the carbon structure were obtained without using any sacrificial templates or an activation process. The effect of pyrolysis temperature on nitrogen doping content, surface area, and pore structures was carefully studied with respect to their effect on different electrochemical behaviors. A carbonization temperature of 900 °C was found to be the most optimal in terms of capacitive performance which was achieved through the balance between a well-developed pore structure, high surface area and moderate nitrogen doping content. The synthesized N-MFCNCs possess superior capacitance in all three of the most commonly used electrolytes – 2 M KCl, 1 M H$_2$SO$_4$ and 6 M KOH – with good retention capability and excellent cycling stability. The capacitance was found to be lower in KCl compared with H$_2$SO$_4$ and KOH electrolytes due to

a lower pseudocapacitance contribution. The best capacitance performance was as high as 352 F g^{-1} at a current density of 5 A g^{-1} when 1 M H$_2$SO$_4$ electrolyte was used. The basicity introduced by N-doping was believed to be particularly beneficial for an enhanced interaction in acidic environment. The well developed porous structure was found to be pivotal for enhancing the double layer capacitance and promoting the pseudocapacitance effect. The work presented here provides an attractive route for the fabrication of high performance capacitive electrode carbon materials through the transformation of cheap, abundant and renewable biomaterials.

Acknowledgements

References

1 W. Gu and G. Yushin, *Wiley Interdiscip. Rev.: Energy Environ.*, 2014, **3**, 424–473.

2 H. Ibrahim, A. Ilinca and J. Perron, *Renewable Sustainable Energy Rev.*, 2008, **12**, 1221–1250.

3 G. Wang, L. Zhang and J. Zhang, *Chem. Soc. Rev.*, 2012, **41**, 797.

4 Y. Zhai, Y. Dou, D. Zhao, P. F. Fulvio, R. T. Mayes and S. Dai, *Adv. Mater.*, 2011, **23**, 4828–4850.

5 L. Wei, M. Sevilla, A. B. Fuertes, R. Mokaya and G. Yushin, *Adv. Funct. Mater.*, 2012, **22**, 827–834.

6 X. Yang, C. Cheng, Y. Wang, L. Qiu and D. Li, *Science*, 2013, **341**, 534–537.

7 D. Pech, M. Brunet, H. Durou, P. Huang, V. Mochalin, Y. Gogotsi, P.-L. Taberna and P. Simon, *Nat. Nanotechnol.*, 2010, **5**, 651–654.

8 X. Ma, L. Gan, M. Liu, P. K. Tripathi, Y. Zhao, Z. Xu, D. Zhu and L. Chen, *J. Mater. Chem. A*, 2014, **2**, 8407–8415.

9 M. Liu, J. Qian, Y. Zhao, D. Zhu, L. Gan and L. Chen, *J. Mater. Chem. A*, 2015, **3**, 11517–11526.

10 Z. Zhao, S. Hao, P. Hao, Y. Sang, A. Manivannan, N. Wu and H. Liu, *J. Mater. Chem. A*, 2015, **3**, 15049–15056.

11 B. Xu, F. Wu, Y. Su, G. Cao, S. Chen, Z. Zhou and Y. Yang, *Electrochim. Acta*, 2008, **53**, 7730–7735.

12 A. S. Arico, P. Bruce, B. Scrosati, J. M. Tarascon and W. Van Schalkwijk, *Nat. Mater.*, 2005, **4**, 366–377.

13 F. Du, D. Yu, L. Dai, S. Ganguli, V. Varshney and A. K. Roy, *Chem. Mater.*, 2011, **23**, 4810–4816.

14 Y. Zhu, S. Murali, M. D. Stoller, K. J. Ganesh, W. Cai, P. J. Ferreira, A. Pirkle, R. M. Wallace, K. A. Cychosz, M. Thommes, D. Su, E. A. Stach and R. S. Ruoff, *Science*, 2011, **332**, 1537–1541.

15 C. Liu, Z. Yu, D. Neff, A. Zhamu and B. Z. Jang, *Nano Lett.*, 2010, **10**, 4863–4868.

16 T. Kwon, H. Nishihara, H. Itoi, Q. H. Yang and T. Kyotani, *Langmuir*, 2009, **25**, 11961–11968.

17 W. Cermignani, T. E. Paulson, C. Onneby and C. G. Pantano, *Carbon*, 1995, **33**, 367–374.

18 D. W. Wang, F. Li, Z. G. Chen, G. Q. Lu and H. M. Cheng, *Chem. Mater.*, 2008, **20**, 7195–7200.

19 C. Wang, Y. Zhou, L. Sun, P. Wan, X. Zhang and J. Qiu, *J. Power Sources*, 2013, **239**, 81–88.

20 J. P. Paraknowitsch and A. Thomas, *Energy Environ. Sci.*, 2013, **6**, 2839.

21 J. P. Paraknowitsch, Y. Zhang, B. Wienert and A. Thomas, *Chem. Commun.*, 2013, **49**, 1208–1210.

22 G. Hasegawa, M. Aoki, K. Kanamori, K. Nakanishi, T. Hanada and K. Tadanaga, *J. Mater. Chem.*, 2011, **21**, 2060–2063.

23 Y. Tan, C. Xu, G. Chen, Z. Liu, M. Ma, Q. Xie, N. Zheng and S. Yao, *ACS Appl. Mater. Interfaces*, 2013, **5**, 2241–2248.

24 Z. Wen, X. Wang, S. Mao, Z. Bo, H. Kim, S. Cui, G. Lu, X. Feng and J. Chen, *Adv. Mater.*, 2012, **24**, 5610–5616.

25 X. Y. Chen, C. Chen, Z. J. Zhang, D. H. Xie, X. Deng and J. W. Liu, *J. Power Sources*, 2013, **230**, 50–58.

26 H. M. Jeong, J. W. Lee, W. H. Shin, Y. J. Choi, H. J. Shin, J. K. Kang and J. W. Choi, *Nano Lett.*, 2011, **11**, 2472–2477.

27 X. Yu, J. Zhao, R. Lv, Q. Liang, C. Zhan, Y. Bai, Z.-H Huang, W. Shen and F. Kang, *J. Mater. Chem. A*, 2015, **3**, 18400–18405.

28 P. Chen, J. J. Yang, S. S. Li, Z. Wang, T. Y. Xiao, Y. H. Qian and S. H. Yu, *Nano Energy*, 2013, **2**, 249–256.

29 J. W. Jeon, R. Sharma, P. Meduri, B. W. Arey, H. T. Schaef, J. L. Lutkenhaus, J. P. Lemmon, P. K. Thallapally, M. I. Nandasiri, B. P. McGrail and S. K. Nune, *ACS Appl. Mater. Interfaces*, 2014, **6**, 7214–7222.

30 Y. H. Lee, Y. F. Lee, K. H. Chang and C. C. Hu, *Electrochem. Commun.*, 2011, **13**, 50–53.

31 L. Li, E. Liu, J. Li, Y. Yang, H. Shen, Z. Huang, X. Xiang and W. Li, *J. Power Sources*, 2010, **195**, 1516–1521.

32 Y. J. Kim, Y. Abe, T. Yanagiura, K. C. Park, M. Shimizu, T. Iwazaki, S. Nakagawa, M. Endo and M. S. Dresselhaus, *Carbon*, 2007, **45**, 2116–2125.

33 Y. Zhao, M. Liu, X. Deng, L. Miao, P. K. Tripathi, X. Ma, D. Zhu, Z. Xu, Z. Hao and L. Gan, *Electrochim. Acta*, 2015, **153**, 448–455.

34 D. Zhu, Y. Wang, L. Gan, M. Liu, K. Cheng, Y. Zhao, X. Deng and D. Sun, *Electrochim. Acta*, 2015, **158**, 166–174.

35 B. Cao, B. Zhang, X. Jiang, Y. Zhang and C. Pan, *J. Power Sources*, 2011, **196**, 7868–7873.

36 J. Zhao, H. Lai, Z. Lyu, Y. Jiang, K. Xie, X. Wang, Q. Wu, L. Yang, Z. Jin, Y. Ma, J. Liu and Z. Hu, *Adv. Mater.*, 2015, **27**, 3541–3545.

37 D. W. Wang, F. Li, L. C. Yin, X. Lu, Z. G. Chen, I. R. Gentle, G. Q. Lu and H. M. Cheng, *Chem.–Eur. J.*, 2012, **18**, 5345–5351.

38 K. Jurewicz, K. Babeł, A. Ziółkowski and H. Wachowska, *J. Phys. Chem. Solids*, 2004, **65**, 269–273.

39 N. D. Kim, W. Kim, J. B. Joo, S. Oh, P. Kim, Y. Kim and J. Yi, *J. Power Sources*, 2008, **180**, 671–675.

40 K. Jurewicz, R. Pietrzak, P. Nowicki and H. Wachowska, *Electrochim. Acta*, 2008, **53**, 5469–5475.

41 A. B. Fuertes and T. A. Centeno, *J. Mater. Chem.*, 2005, **15**, 1079.

42 H. Konno, H. Onishi, N. Yoshizawa and K. Azumi, *J. Power Sources*, 2010, **195**, 667–673.

43 S. Shrestha and W. E. Mustain, *J. Electrochem. Soc.*, 2010, **157**, B1665.

44 C. O. Ania, V. Khomenko, E. Raymundo-Piñero, J. B. Parra and F. Béguin, *Adv. Funct. Mater.*, 2007, **17**, 1828–1836.

45 G. Lota, K. Lota and E. Frackowiak, *Electrochem. Commun.*, 2007, **9**, 1828–1832.

46 E. Raymundo-Piñero, F. Leroux and F. Béguin, *Adv. Mater.*, 2006, **18**, 1877–1882.

47 Z. Li, L. Zhang, B. S. Amirkhiz, X. Tan, Z. Xu, H. Wang, B. C. Olsen, C. M. B. Holt and D. Mitlin, *Adv. Energy Mater.*, 2012, **2**, 431–437.

48 X. L. Wu, T. Wen, H. L. Guo, S. Yang, X. Wang and A. W. Xu, *ACS Nano*, 2013, **7**, 3589–3597.

49 T.-D. Nguyen, K. E. Shopsowitz and M. J. MacLachlan, *J. Mater. Chem. A*, 2014, **2**, 5915–5921.

50 C. Long, D. Qi, T. Wei, J. Yan, L. Jiang and Z. Fan, *Adv. Funct. Mater.*, 2014, **24**, 3953–3961.

51 L.-F. Chen, Z.-H. Huang, H.-W. Liang, W.-T. Yao, Z.-Y. Yu and S.-H. Yu, *Energy Environ. Sci.*, 2013, **6**, 3331.

52 L. Zhao, L. Z. Fan, M. Q. Zhou, H. Guan, S. Qiao, M. Antonietti and M. M. Titirici, *Adv. Mater.*, 2010, **22**, 5202–5206.

53 T. Asefa, *Angew. Chem., Int. Ed.*, 2012, **51**, 2008–2010.

54 M. D. Stoller and R. S. Ruoff, *Energy Environ. Sci.*, 2010, **3**, 1294.

55 Y. Wu, Y. Li, L. Qin, F. Yang and D. Wu, *J. Mater. Chem. B*, 2013, **1**, 204–212.

56 R. J. Nemanich and S. A. Solin, *Phys. Rev. B: Condens. Matter Mater. Phys.*, 1979, **20**, 392–401.

57 X. Xiao, T. E. Beechem, M. T. Brumbach, T. N. Lambert, D. J. Davis, J. R. Michael, C. M. Washburn, J. Wang, S. M. Brozik, D. R. Wheeler, D. B. Burckel and R. Polsky, *ACS Nano*, 2012, **6**, 3573–3579.

58 D. Hulicova, J. Yamashita, Y. Soneda, H. Hatori and M. Kodama, *Chem. Mater.*, 2005, **17**, 1241–1247.

59 T. Hirata, S. Kawamoto and A. Okuro, *J. Appl. Polym. Sci.*, 1991, **42**, 3147–3163.

60 C. Devallencourt, J. Saiter, A. Fafet and E. Ubrich, *Thermochim. Acta*, 1995, **259**, 143–151.

61 P. K. Tripathi, M. Liu, Y. Zhao, X. Ma, L. Gan, O. Noonan and C. Yu, *J. Mater. Chem. A*, 2014, **2**, 8534–8544.

62 T. Li, G. Yang, J. Wang, Y. Zhou and H. Han, *J. Solid State Electrochem.*, 2013, **17**, 2651–2660.

63 D. W. Wang, F. Li, M. Liu, G. Q. Lu and H. M. Cheng, *Angew. Chem., Int. Ed.*, 2008, **47**, 373–376.

64 E. Paek, A. J. Pak, K. E. Kweon and G. S. Hwang, *J. Phys. Chem. C*, 2013, **117**, 5610–5616.

65 L.-F. Chen, X.-D. Zhang, H.-W. Liang, M. Kong, Q.-F. Guan, P. Chen, Z.-Y. Wu and S.-H. Yu, *ACS Nano*, 2012, **6**, 7092–7102.

66 J. Han, G. Xu, B. Ding, J. Pan, H. Dou and D. R. MacFarlane, *J. Mater. Chem. A*, 2014, **2**, 5352–5357.

67 J. Hou, C. Cao, F. Idrees and X. Ma, *ACS Nano*, 2015, **9**, 2556–2564.

23776 | *J. Mater. Chem. A*, 2015, **3**, 23768–23777

This journal is © The Royal Society of Chemistry 2015

68 G. Lota, K. Lota and E. Frackowiak, *Electrochem. Commun.*, 2007, **9**, 1828–1832.
69 A. Burke, *Electrochim. Acta*, 2007, **53**, 1083–1091.
70 B. E. Conway, *Electrochemical Supercapacitors: Scientific Fundamentals and Technological Applications*, Springer Science & Business Media, 2013.

71 A. J. Bard and L. R. Faulkner, *Electrochemical Methods: Fundamentals and Applications*, 2001.
72 E. Frackowiak and F. Beguin, *Carbon*, 2001, **39**, 937–950.
73 B. Hsia, M. S. Kim, C. Carraro and R. Maboudian, *J. Mater. Chem. A*, 2013, **1**, 10518–10523.